ADVANCED MATERIALS TECHNOLOGIES
www.advmattechnol.de

Highly Sensitive and Integratable Triboelectric Bionic Lateral Line Sensor for Flow Recognition of Underwater Vehicle

Jianhua Liu, Bo Liu, Ziyue Xi, Hengyi Yang, Yuanzheng Li, Hengxu Du, Zhaoyang Mu, Jicang Si, Siyuan Wang, Peng Xu,* and Minyi Xu**

The ability to perceive underwater flow fields is essential for the stable operation and efficient navigation of underwater vehicles. Fish use their lateral lines to detect changes in the surrounding flow field, even in low visibility and harsh environments. Inspired by the lateral line neuromasts of fish, this paper introduces a triboelectric bionic lateral-line sensor (TBLS) designed to enable underwater vehicles to detect flow fields, including propeller-generated wakes and oscillating flows. The TBLS comprises a flexible sensing unit and a bionic lateral-line canal. It has a measurement error of just 5.7% in determining the characteristic thickness of propeller wakes and has a pressure gradient sensitivity of 2.1 mV Pa m^{-1}. The H2O AutoML algorithm significantly enhances the recognition of oscillatory flow signals. Finally, the TBLS is integrated into an underwater vehicle, demonstrating its ability to detect underwater flow fields and transmit signals 117 meters to a receiving end via a wireless transmission module in real-sea conditions. The TBLS provides a novel approach to enhancing flow field perception and underwater operational capabilities of vehicles.

1. Introduction

With advancements in artificial intelligence and underwater vehicle technology, the coordinated operation of underwater unmanned systems plays a critical role in marine resource exploration, environmental monitoring, and maritime rescue.[1–5] However, the complexity of underwater environments often presents significant challenges for these vehicles in executing tasks.[6–8] Accurate flow field perception is essential for their effective operation. While acoustic sensors have traditionally been the primary method for flow field perception, their performance can be hindered by seafloor irregularities and substrate heterogeneity.[9,10] Optical sensors are also commonly used for underwater detection due to their high sensitivity. However, their reliability and stability are affected by waterborne impurities and particle granularity.[11,12] To address these limitations, researchers are investigating hydrodynamic field-based sensing technologies to enhance the capability of underwater vehicles in measuring and analyzing flow field characteristics.

The concept of bionics is highly significance for researchers involved in sensor structure design and material property optimization. Bionic-based sensors have been widely developed for applications in wearable electronic devices, human-computer interaction, and other critical fields.[13,14] Therefore, drawing inspiration from bionic principles can drive innovation in sensor design and enhance performance. Marine organisms have developed extraordinary sensory systems through their long evolutionary process.[15–18] Inspired by these systems, researchers have designed various sensors based on the whisker structures of marine organisms.[19–21] These sensors enable the detection of underwater obstacles[22] and the wake generated by fish tails.[23] Sarah et al. designed a bionic seal whisker sensor that can be integrated into an unmanned boat.[24] This sensor detects changes in water current direction and assesses the boat's motion. Additionally, the lateral line of fish consists mainly of superficial neuromasts and canal neuromasts (CN). Specifically, CN primarily detects pulsating pressure.[25,26] This sensory system plays a crucial role in feeding and predator avoidance predators in low-light marine environments.[27] The unique sensing capabilities of the lateral line provide valuable insights for designing bionic lateral line sensors.[28] Based on this concept, Shu et al. utilized polyvinylidene fluoride to design artificial lateral line sensors capable of detecting water flow changes and imaging electric fields.[29] However, the fabrication process of this sensor is complex, and its performance in challenging sea conditions requires further investigation. Compared to these sensors, researchers have developed structurally simpler and more cost-effective sensors with good sensing performance.[30,31] However, relatively few have been

J. Liu, B. Liu, Z. Xi, Y. Li, H. Du, Z. Mu, J. Si, S. Wang, P. Xu, M. Xu
State Key Laboratory of Maritime Technology and Safety
Marine Engineering College
Dalian Maritime University
Dalian 116026, China
E-mail: wsydlmu@dlmu.edu.cn; pengxu@pku.edu.cn; xuminyi@dlmu.edu.cn
H. Yang
School of Engineering
Newcastle University
Newcastle upon TyneNE1 7RU, UK
P. Xu
Intelligent Biomimetic Design Lab, College of Engineering
Peking University
Beijing100871, China

The ORCID identification number(s) for the author(s) of this article can be found under https://doi.org/10.1002/admt.202500072

DOI: 10.1002/admt.202500072

applied in underwater environments. Therefore, there is an urgent need for a sensor design solution with good sensing capability and adaptive performance to consider the above requirements.

Triboelectric nanogenerators (TENGs) are an emerging electromechanical conversion technology capable of directly transforming mechanical motion on a device's surface into electrical signals.[32–35] Their primary advantage lies in their high sensitivity to micro-perturbations, enabling effective sensing of physical quantities such as dynamic pressure,[36] vibration,[37,38] and rotation.[39,40] Underwater sensors based on TENGs have been applied in marine applications,[41–43] including liquid level sensing,[44,45] paddle force direction sensing,[46] biological posture monitoring,[47] and underwater environmental monitoring.[48,49] Additionally, researchers have investigated integrating underwater vehicles with triboelectric sensors. Xu et al. designed a bionic palm tactile sensor mounted on an underwater robotic manipulator for pipeline leak detection.[50] However, research on triboelectric bionic lateral-line sensor designed to enhance underwater vehicles perception of multiple flow fields in low- visibility conditions remains limited.

This paper presents a triboelectric bionic lateral-line sensor (TBLS) designed for integration with underwater vehicles to facilitate flow field recognition. The TBLS innovatively combines the tactile perception mechanism of the fish lateral line with the principle of TENGs. When detecting disturbances in the external flow field, its flexible sensing unit generates corresponding electrical signals. Experimental results demonstrate that the TBLS can sense and characterize the wake generated by a propeller in motion. Even in low-light conditions, it aids remotely operated vehicle (ROV) in sensing and locating underwater disturbances sources. Additionally, the TBLS effectively detects oscillatory flows achieving a sensitivity of 2.1 mV Pa m^{-1} for pressure gradients, while the H2O AutoML algorithm attains 100% accuracy in recognizing different oscillatory flow signals. Finally, we constructed a monitoring platform, and the underwater disturbance information sensed by TBLS can be sent to the receiver 117 meters away via the wireless transmission module on an unmanned surface vessel (USV). This significantly enhances the ROV's capability for underwater flow field sensing.

2. Results and Discussion

2.1. Basic Structure and Working Mechanism of the TBLS

The lateral line system plays a crucial role in fish behavior, even in low-light environments. Its primary distribution locations are shown in **Figure** 1a-i. Figure 1a-ii illustrates CN of the lateral line, which detect pressure changes and subtle vibrations in water through pressure differences between adjacent pores. CN include the cupula, sensory hairs, sensory hair cells, and nerves, as shown in Figure 1a-iii. When water flow or vibrations displace the cupula, the sensory hairs bend in response. Ca^{2+} ions to pass through open ion channels, thereby altering the electrical signals in the hair cell, as depicted in Figure 1b. Inspired by the CN sensing mechanism of the lateral line, a TBLS was designed. This TBLS consists of a bionic lateral-line pipeline measuring 100 mm × 200 mm × 90 mm, with a pipeline aperture of 50 mm, and a flexible sensing unit, as shown in Figure 1c.

As shown in Figure 1d, the internal structure of the flexible sensing unit (50 mm × 18 mm) consists of ink, fluorinated ethylene propylene (FEP), cast polypropylene (CPP), and silicone rubber. Specifically, the FEP is polished to increase the contact area, thereby enhancing charge transfer. Field emission scanning electron microscopy was used to characterize the FEP surface morphology, as shown in Figure S3 (Supporting Information). CPP ensures the signal-to-noise ratio of the flexible sensing unit through its electrostatic shielding properties. Silicone rubber provides waterproofing. The sensing principle of the flexible sensing unit is illustrated in Figure 1e. When the TBLS detects a changes in external dynamic pressure, the pressure difference between the front and rear holes causes the flexible sensing unit to deflect. This deflection brings the dielectric layer into contact with the electrode layer on one side, generating opposite charges on the surfaces of the two materials via the triboelectric effect. The FEP surface becomes negatively charged, while the ink becomes positively charged. When the dielectric layer separates from the electrode layer, a positive charge is generated at the opposite electrode due to the flow of free electrons in the external circuit, balancing the potential difference. Under the influence of external dynamic pressure, the flexible sensing unit continues to deflect. The charge transfers completely upon contact of the dielectric layer with the electrode layer on the other side. Subsequently, the flexible sensing unit returns to its neutral position, causing the charge to undergo reverse transfer and generating an opposite output signal. Through an analysis of the structural design and operational principles of the flexible sensing unit, we employed COMSOL Multiphysics software to simulate and analyze the electric potential distribution during its sensing process. By establishing a model of the sensing unit and configuring material types and relevant parameters, we obtained the electric potential distribution of the TBLS's flexible sensing unit across various stages, depicted in Figure 1f. Figure 1g illustrates the potential application of TBLS in marine environment sensing. By constructing an ROV-USV underwater monitoring platform with TBLS, a novel approach to monitoring the marine environment has been realized. This system senses the underwater environment and transmits the information in real time through wireless transmission.

2.2. Electrical Characterization of the TBLS

To evaluate the wake perception capability of the TBLS, we constructed an intelligent experimental pool (4.0 m × 6.0 m × 1.5 m) equipped with an underwater towing system, an underwater camera system, and a signal acquisition system, as shown in **Figure** 2a. The trailing guide moves along a predefined route at speeds ranging from 0.1 to 0.5 ms^{-1}, enabling the study of the temporal and spatial characteristics of TBLS wake perception. The TBLS was mounted on the vertical axis of the towing beam and towed in the direction indicated in Figure 2b, simulating an operational underwater vehicle equipped with the TBLS. A submerged propeller served as the propulsion device of another underwater vehicle. Figure 2c shows in magnification the relative position of the propeller fixed to the aluminum profile frame

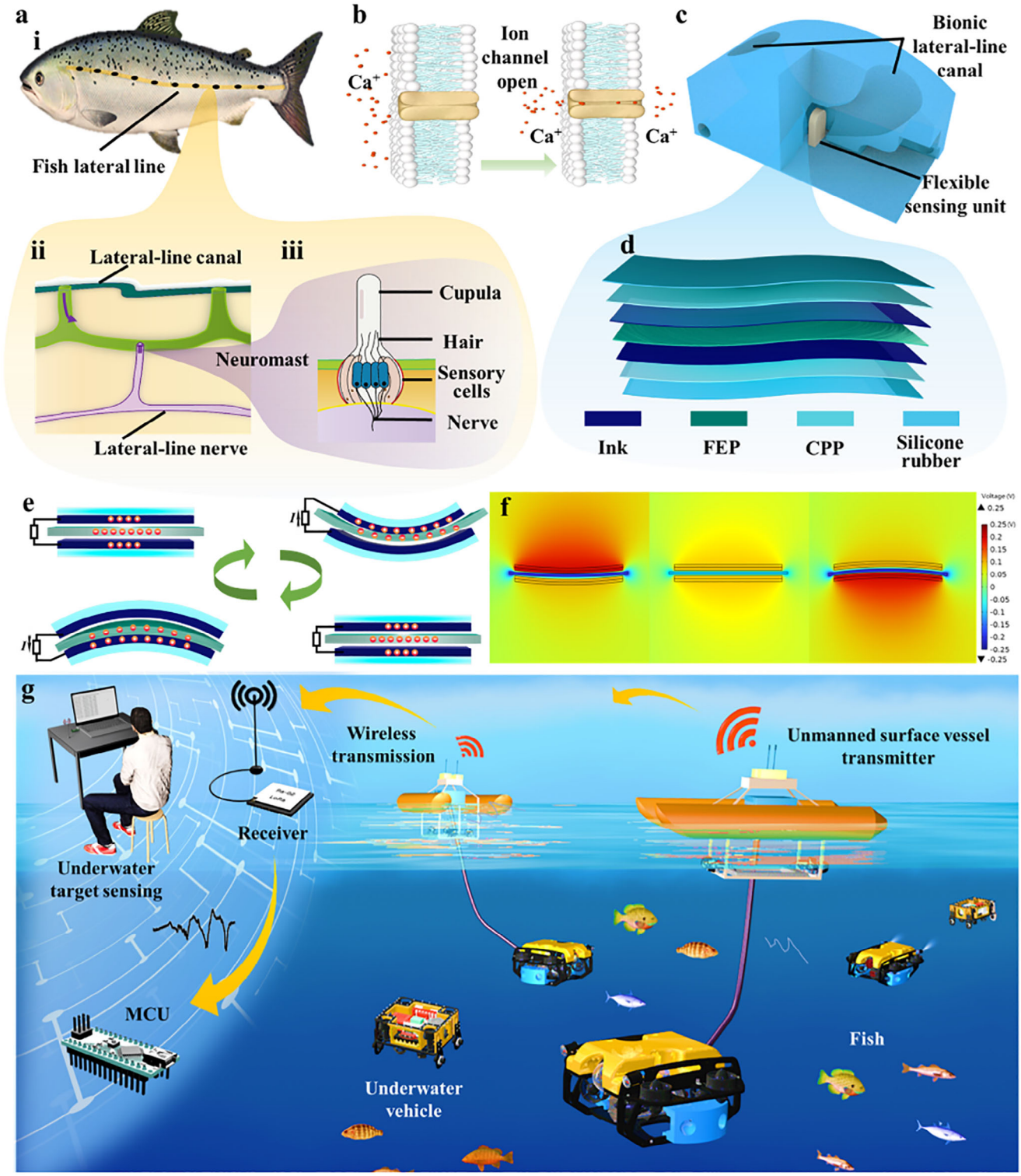

Figure 1. Structural design and application of the TBLS. a) Lateral-line system of fish. i) Main distribution position. ii) Perception mechanism. iii) Neuronal structure within the lateral-line canal. b) Ion channel diagram. c) Structural diagram of the TBLS. d) Internal structure of flexible sensing unit. e) Working mechanism of TBLS. f) Electric potential distribution of TBLS. g) Application diagram of the TBLS.

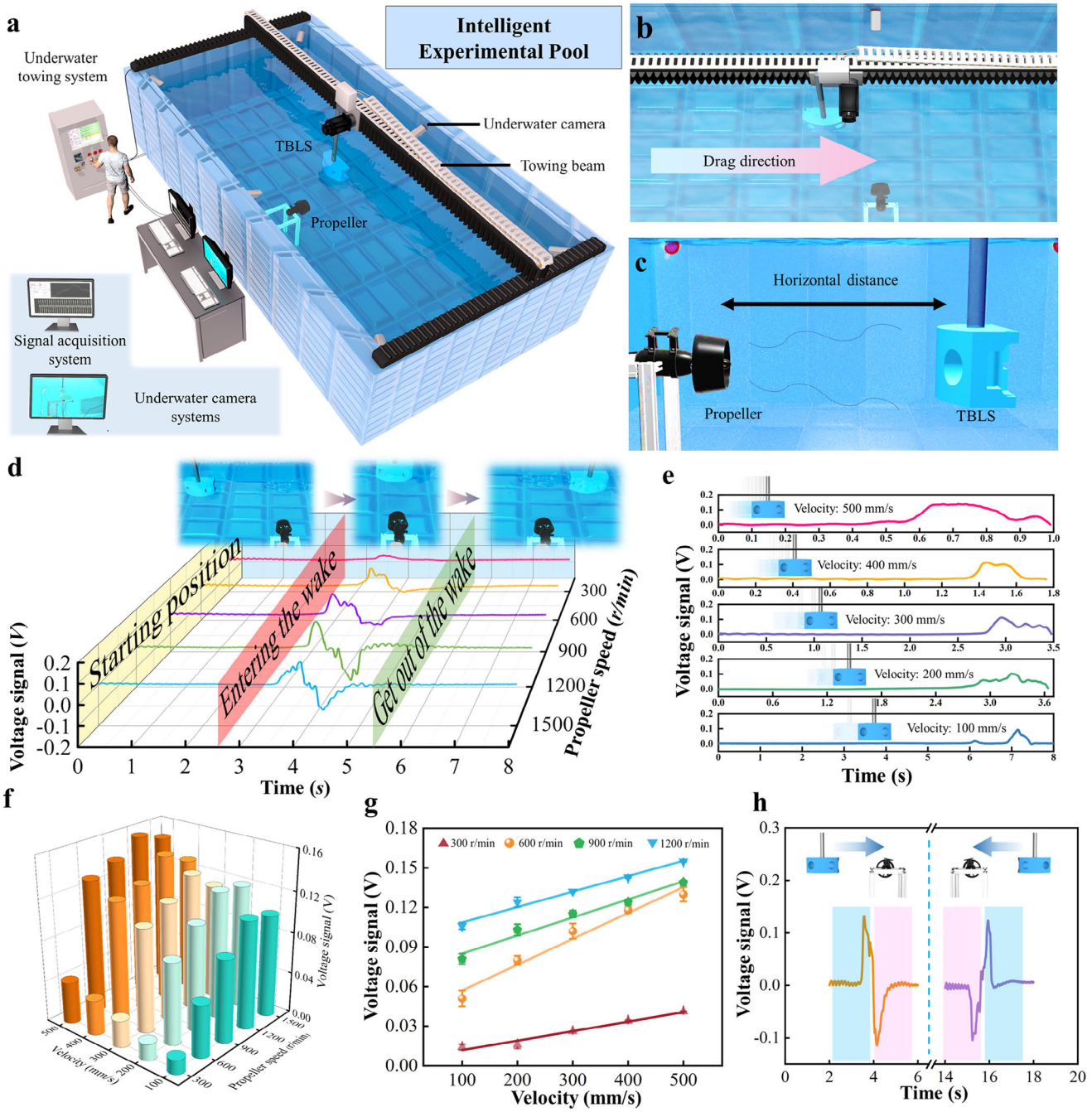

Figure 2. Electrical characterization of TBLS for towing experiments. a) Schematic diagram of intelligent experimental pool. Schematic diagram of b) TBLS towing experiment and c) experimental setup. d) The open-circuit voltage corresponding to the propeller speed from 300 to 1500 r/min. e) The open-circuit voltage corresponding to the towing velocity from 0.1 to 0.5 ms^{-1}. f) The distribution of the open-circuit voltage with respect to the propeller speed and the towing velocity. g) Linear fitting between open-circuit voltage and towing speed at different propeller speeds. h) The relationship between towing direction and open-circuit voltage.

concerning the TBLS. This helps to clearly understand the study proposed below on the effect of horizontal distance on the perception characteristics of the TBLS. In this study, various motion states of the underwater vehicle were simulated by adjusting the propeller's rotation speed. The wake perception characteristics of the TBLS were analyzed at a towing speed of 0.3 ms^{-1} and a horizontal distance of 85 cm.

Figure 2d illustrates the voltage variation of the TBLS under different propeller speeds. The towing process is divided into three distinct intervals: the start time (yellow), entering the wake (red), and leaving the wake (green). As the underwater towing system begins, the TBLS moves at a constant speed of 0.3 ms^{-1}. At 2.7 s, the front-side hole of the TBLS senses the wake, generating a pressure difference between the two holes, which deforms

the internal sensing unit and leads to a rising voltage signal. As the system progresses, the rear-side hole of the TBLS senses the wake, creating an opposite pressure difference, and the voltage signal shows a falling edge. At 5.5 s, the TBLS exits the wake, the sensing unit returns to its initial state, and the signal stabilizes. The accompanying diagram in Figure 2d shows the TBLS at three positions relative to the propeller. Specifically, at a propeller speed of 300 r min^{-1}, the peak voltage of the TBLS's rising edge is 0.026 V. As the propeller speed increases, the TBLS's electrical signal also rises, reaching 0.132 V at 1200 r min^{-1}. However, further increasing the propeller speed to 1500 r min^{-1} decreased the TBLS signal, as the sensing unit exceeded its deflection range.

Understanding the applicability of TBLS at different towing speeds is crucial given the varying operational speeds of underwater vehicles. Figure 2e examines the TBLS's wake perception capability under different towing speeds. The experiments systematically varied the towing platform's speed from 0.1 to 0.5 ms^{-1} to assess how the underwater vehicle perceives the wake generated by a propeller operating at 900 r min^{-1} across different velocities. Only the signal generated when the front-side hole passed through the wake area was analyzed. The TBLS's wake perception capability was evaluated based on the characteristics of this signal. At the towing velocity of 0.1 ms^{-1}, the TBLS produces a distinct peak signal with a voltage of 0.081 V at 7.0 s. As the towing velocity increases, the voltage gradually rises, and the signal generation time shortens. At a towing speed of 0.5 ms^{-1}, the voltage reaches 0.139 V. This demonstrates the TBLS's ability to effectively sense wakes across a wide range of operating velocities. Additional tests were conducted at other propeller speeds, as shown in Figure 2f. The data indicate that at a propeller speed of 1500 r min^{-1}, the TBLS deviates from the previously observed gradual growth trend. Reaffirming its effective sensing range. Therefore, subsequent experiments were conducted within the validated test conditions. The linear fit relationship between voltage and towing velocity is illustrated in Figure 2g. All correlation coefficients exceed 0.9, indicating a robust linear relationship between the voltage and the towing velocities. As the front and rear holes of the TBLS sequentially passed through the wake region, the TBLS generates two distinct signal peaks: a rising edge followed by a falling edge. To assess whether the TBLS can determine its movement direction relative to the wake region, electrical signals generated by the TBLS in different moving directions were analyzed, as shown in Figure 2h. When moving from left to right, the TBLS first produces a rising edge (blue) followed by a falling edge (pink). Conversely, the signal waveform displays a falling edge first, followed by a rising edge. These results confirm that the TBLS can identify the movement direction of the underwater vehicle based on signal waveform changes.

We used Ansys to simulate the propeller wake. **Figure 3**a illustrates the 2D velocity contours of the wake. The velocity is highest in the red region near the wake's source, decreasing with distance, and gradually changing to blue. The velocity contours spread downstream from the wake's source, progressively lightening in color. Higher velocities in the center of the wake gradually spread outward and weaken. Figure 3b demonstrates the radial distribution of wake intensity from a front-facing perspective of the propeller. The figure shows the velocity distributed in concentric circles from the center outward, with the color gradually lightening, indicating that the velocity decays as it diffuses radially. To verify the TBLS's sensing effect on the wake of the underwater vehicle's propulsion device, a 3D coordinate system was established in the intelligent experimental pool. Figure 3c shows the top view of the pool and the established XY coordinate system in this plane. In this system, the pool's bottom horizontal line represents the x-axis, the left side represents the y-axis, and their intersection serves as the coordinate origin. At a propeller speed of 900 r min^{-1}, the TBLS moves along the positive x-axis at 0.2 ms^{-1}. Wake sensing tests were conducted at five horizontal distances (H_1-H_5).

Figure 3d shows the relationship between the horizontal distance and the electrical signal generated by the TBLS. When the horizontal distance is 35 cm, the TBLS detects the wake after moving along the positive x-axis for 2.42 s. At this point, its front-side hole enters the wake region first, generating a rising-edge peak signal of 0.168 V. As the TBLS continues to move, the rear-side hole enters the wake area, generating a distinct falling-edge peak signal of ≈0.127 V. At a horizontal distance of 60 cm, the TBLS generates a voltage signal of 0.134 V at 2.31 s after the start of its movement. The perceptual characteristics of the TBLS at different horizontal distances were studied. The results indicate that as the horizontal distance increases to 135 cm, the perceived signal intensity weakens significantly. However, the time at which the TBLS senses the signal gradually advances. As the horizontal distance increases, the wake intensity gradually weakens, resulting in a decrease in the amplitude of the electrical signal. Nevertheless, the wake's diffusion enables earlier detection by the TBLS. Notably, the heatmap depicting the relationship between horizontal distance and electrical signals closely resembles the "flare mouth" shape observed in the propeller wake simulation results in Figure 3a. The characteristic thickness of the main cross-section of the free turbulent jet generated by the propeller is calculated by[51]

$$\frac{b}{x} = \tan\theta = c \tag{1}$$

where, θ is the angle between the jet boundary and the axis, and the constant $c = 0.114$. In the case of $H = 85$ cm, the theoretical characteristic wall thickness $b = 0.194$ m can be derived from (1). The actual measured feature thickness $b = 0.205$ m is derived from the peak signal period and drag speed generated by the TBLS in Figure 3d, with a measurement error rate of 5.7%. Therefore, the TBLS proved to have a good perception of the wake field generated by the propeller.

Subsequently, we tested the TBLS's ability to sense wake at different heights. Figure 3e establishes the XZ plane coordinate system in the main view direction. The symmetry of the wake can be seen from the simulation results in Figure 3b, so only four height positions (V_1-V_4) along the positive half of the z-axis are tested. Under the same conditions as the previous experiment, the vertical height of the TBLS was adjusted along the z-axis of the towing device at a horizontal distance of 85 cm from the propeller. The TBLS generated a voltage of ≈0.1 V at $z = 0$ cm. As the vertical height increased to 15 cm, the voltage decreased to ≈0.01 V. The voltage gradually weakened as the vertical height from the propeller increased. The simulation results in Figure 3b accurately reflect that the intensity of the wake generated by the propeller gradually spreads and weakens from the center to the

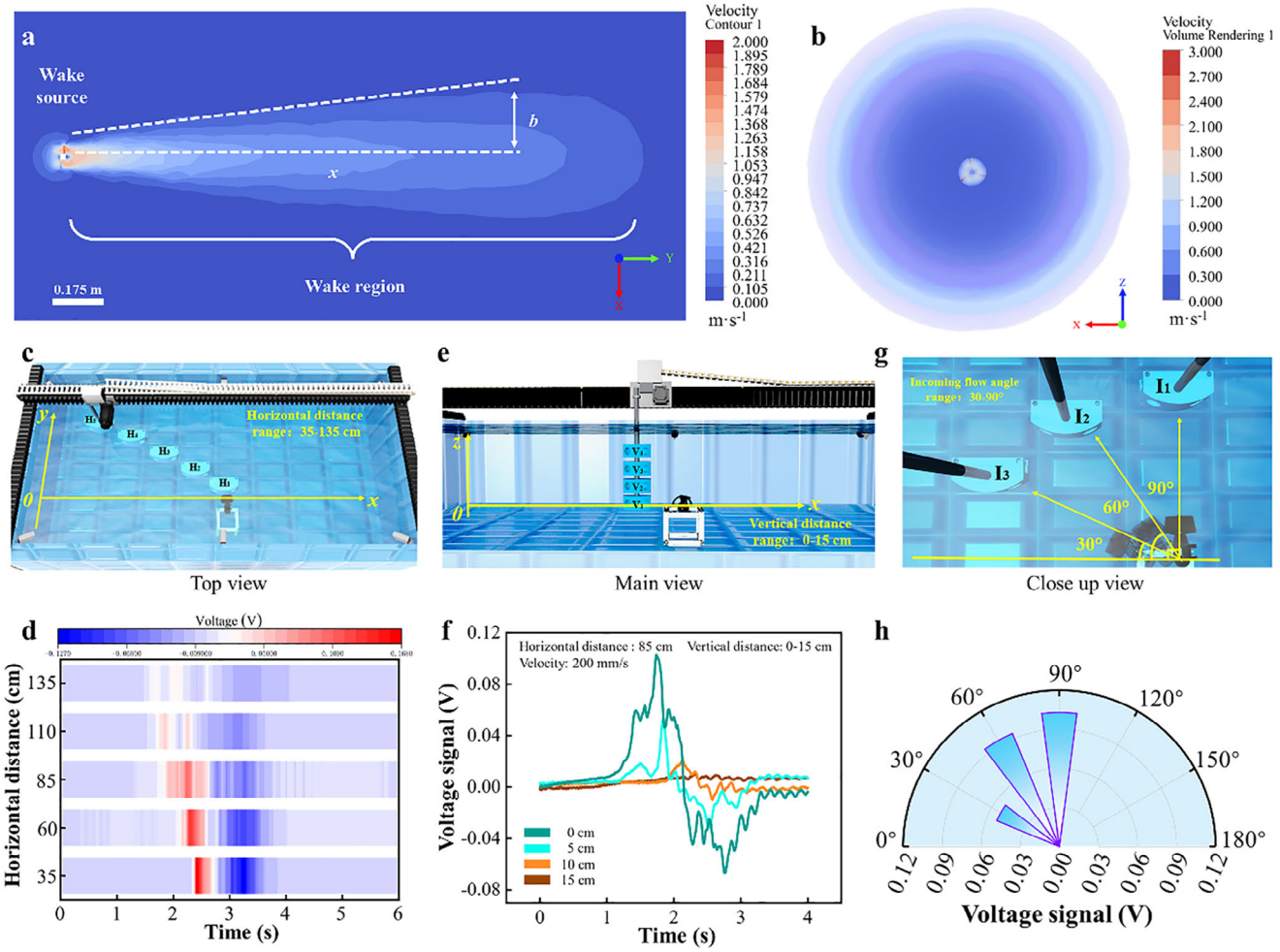

Figure 3. Electrical characterization and simulation of TBLS. a) 2D state simulation of propeller wake characteristics. b) Simulation of radial distribution characteristics of propeller wake. Schematic of c) the TBLS at different horizontal distances from the propeller and d) the corresponding open-circuit voltages. Schematic of e) the TBLS at different vertical distances from the propeller and f) the corresponding open-circuit voltages. Schematic diagrams of g) the TBLS with different incoming flow angles from the propeller and h) the corresponding open circuit voltages.

surrounding areas. The signal detected by the TBLS strongly responded to the propeller wake. Polynomial fitting reveals a correlation between the two as $U = -0.0004z^2 - 0.012z + 0.1$. As the height increased, the voltage signal showed a decreasing trend. Figure S4 (Supporting Information) illustrates the U-z model's detection accuracy and generalization ability, showing that the quadratic function of output voltage and vertical distance fits well, with a correlation coefficient close to 1. In practical environments, the diverse movement directions of underwater vehicles often render the direction of the propeller wake uncertain. This study examined the relationship between the TBLS sensing signal and the relative angle of the propeller at $x = 85$ cm, $z = 0$ cm, as depicted in Figure 3g. Figure 3h presents the test results conducted at three incoming flow angles (I_1, I_2, and I_3). As the TBLS moved from position I_1 to position I_3, the voltage dropped from 0.1 to 0.05 V. This indicates that the TBLS also possesses the ability to discern the direction of incoming flow.

Hydrodynamic disturbances caused by the movements of marine organism appendages typically result in underwater oscillatory flows.[52] An experimental platform for underwater dipole oscillation was constructed to assess the TBLS's capability in detecting underwater oscillatory flows. The right portion of **Figure** 4a illustrates the experimental setup, which includes the pendant linear motor and the oscillating dipole. The underwater oscillating flow is simulated by the reciprocating motion of the oscillating dipole. The two illustrations on the left side of Figure 4a depict the underwater view of the oscillating dipole at its starting and ending positions. Figure 4b examines the oscillation frequency and displacement sensing performance of the TBLS with the oscillating dipole. According to the dipole model, the pressure gradient between adjacent holes can be determined, as stated in,[53]

$$\frac{dp}{dx} = \left(\frac{1}{D^2} - \frac{1}{\left(D^2 + (\Delta x)^2\right)^{3/2}} \right) \frac{\rho r^3}{2\Delta x} A_s \sin\left(2\pi f t\right) \quad (2)$$

where f is the vibration frequency of the sphere, A_s is the acceleration amplitude of the sphere, r is the radius of the sphere, D is the distance from the sphere to the hole. Figure 4c illustrates the relationship between the TBLS voltage signal and the oscillation

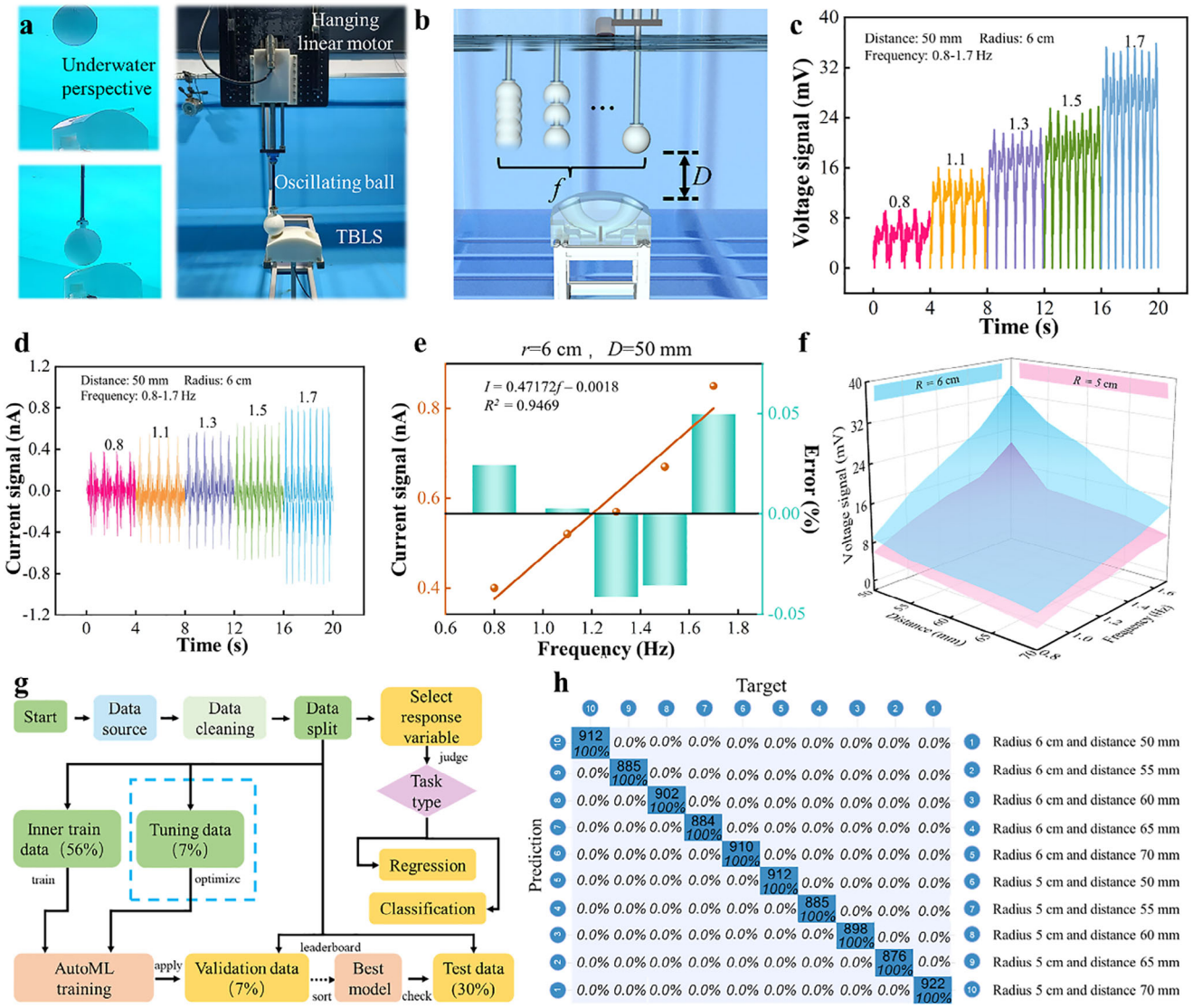

Figure 4. Electrical characterization of the TBLS in the oscillating flow. a) Experimental setup. b) Schematic diagram of experimental test. c) The open-circuit voltage corresponding to the oscillation frequency from 0.8 to 1.7 Hz. d) The short-circuit current corresponding to the oscillation frequency from 0.8 to 1.7 Hz. e) Fitting linear relationship between short-circuit current and oscillation frequency. f) Relationship between oscillation frequency and distance and open-circuit voltage under different radius oscillating sphere conditions. g) Outline Flowchart. h) Classification and identification results.

frequencies, measured with a dipole radius of 6 cm and an oscillation amplitude of 50 mm. At an oscillation frequency of 0.8 Hz, the TBLS voltage signal is 9.4 mV. As the frequency increases to 1.7 Hz, the voltage signal rises to 35.2 mV. The increase in oscillation frequency leads to greater deformation of the flexible sensing unit. This deformation results in a larger contact area between the FEP and ink, which enhances the charge transfer. Consequently, this increased charge transfer produces a larger voltage. The relationship between the voltage and the oscillation frequency was determined by linear fitting. The fitted relationship is $U = 27.4959f - 13.6147$, and the linear correlation coefficient R^2 is 0.97169, as shown in Figure S5 (Supporting Information). The relationship between the TBLS current and various frequencies of the oscillating dipole was examined. Figure 4d shows that the TBLS current signal increases from 0.38 to 0.81 nA as the oscillation frequency rises. Similarly, Figure 4e presents the results of fitting the linear relationship between the TBLS current signal and oscillation frequency. The fitted equation is $I = 0.47172f - 0.0018$, with a linear correlation coefficient R^2 of 0.9469. Both voltage and current signals exhibit strong linear correlations with oscillation frequency (correlation coefficients greater than 0.94). Therefore, the TBLS effectively senses external oscillation frequencies through both electrical signals.

Additionally, Figure S6 (Supporting Information) shows the relationship between the voltage and the oscillating dipole at different distances when the oscillation frequency is 1.7 Hz. The voltage increased from 9.4 to 35.2 mV as the distance between the oscillating dipole and the TBLS decreased from 70 to 50 mm. In

the case of $D = 50$ mm, $r = 6$ cm, and $\Delta x = 130$ mm, the theoretical hydrodynamic pressure gradient is 16.8 Pa m^{-1} as calculated in equation (2). The TBLS's detection sensitivity to the pressure gradient is 2.1 mV Pa m^{-1}, which is three orders of magnitude higher than that reported in previous studies.[36] The relationship between the voltage and distance is described by the equation $U = -1.048D + 85.84$, with a high linear correlation coefficient $R^2 = 0.96271$, as shown in Figure S7 (Supporting Information). Figure S8a–d (Supporting Information) show the voltage at different oscillation frequencies, with distances ranging from 55 to 70 mm. All fitting results indicate strong correlations, as shown in Figure S8e–h (Supporting Information). To assess the TBLS's response to oscillating dipoles of varying radii, an oscillating dipole with a 5 cm radius was tested, as shown in Figure S8i (Supporting Information). The voltage increased with both higher oscillation frequencies and shorter distances. Figure 4f analyzes the perceptual characteristics of oscillating dipoles of different radii under various conditions, providing a clearer understanding of the TBLS's sensitivity to oscillating flow. The data show that the voltage signal increases with decreasing oscillation distance and increasing oscillation frequency. Furthermore, a larger dipole radius results in a higher voltage signal.

To enhance the TBLS's ability to perceive the oscillatory flow in various states, we utilized H2O AutoML to construct a classification model for signal recognition. H2O AutoML offers an efficient and user-friendly automated machine learning solution. Figure 4g illustrates the process used in the oscillatory flow state sensing experiment. Initially, data cleaning was performed on the experimental base data before training. During the training phase, H2O AutoML automatically filters out irrelevant data based on quality metrics. The dataset was then split into training and test sets in a 70:30 ratio. Specifically, the training set was further divided into inner training, tuning, and validation sets in an 80:10:10 ratio. The tuning set was utilized to adjust hyperparameters for each model to prevent overfitting or underfitting. After data entry, H2O AutoML completed model training and hyperparameter tuning autonomously, selecting the optimal model. Training was terminated when either the maximum run time or the maximum number of models was reached. All internally trained models were evaluated on the validation set, and a leaderboard of models was generated to identify the best performer. This selected model was then used for classification and recognition tasks. The test data was reserved solely for evaluation and was neither used directly nor indirectly during model training. The maximum runtime for each model was set to 20 min, with deviation as the stopping criterion. The predictions generated through this automated machine learning approach are shown in Figure 4h. Notably, the model accurately classified ten oscillatory flow scenarios with a recognition accuracy of 100%. This approach significantly improved the accuracy of the TBLS for detecting underwater oscillatory flows compared to traditional fitting methods.

2.3. Demonstration of TBLS-Based Flow Field Recognition for ROV

To further verify the ability of TBLSs to assist an ROV in sensing field flows, TBLSs were integrated on both sides of the ROV, as shown in **Figure 5a**, with a more detailed presentation in Figure S9 (Supporting Information). Typically, the effectiveness of visual sensors, the primary means of underwater perception, depends on environmental light conditions. TBLS provides an alternative sensing method for ROVs operating in harsh environments. An experimental scenario was designed to evaluate the TBLS's perceive underwater flow field capabilities for, depicted in Figure 5b. The ROV equipped with TBLS started from a position near the coordinate origin, with an underwater propeller located to the northeast. Figure 5c-i depicts the ROV's visual range under favorable lighting conditions, where it has sufficient visibility to observe objects with high precision. In contrast, Figure 5c-ii,iii show the ROV's visible range in darkness, where it must rely solely on its onboard lights. However, limited lighting results in a restricted visual range. Therefore, equipping the ROV with TBLS is essential for overcoming these limitations.

Figure 5d illustrates the process of wake sensing under dark conditions using TBLS. Initially, the blue region represents a stationary state, during which no significant fluctuations are observed in the TBLS signal. The ROV then moves along the positive x-axis direction. The ROV commences motion at ≈11.2 s, as indicated in the enlarged inset. The green region denotes the ROV's constant-speed phase, during which the voltage remains stable, confirming that uniform motion does not interfere with the sensor's ability to monitor the wake. At 26.5 seconds, the TBLS on the left side shows a noticeable waveform change., marking the ROV's entry into the wake region (yellow) and generating a 0.01 V signal. Figure 5c-ii shows the light reflection caused by the ROV's illumination lamp on the pool wall during this time. As the ROV advances toward the wake source, the TBLS voltage increases to 0.03 V (red), signifying closer proximity. Subsequently, the ROV detects the underwater propeller through its illumination system, as depicted in Figure 5c-iii. The vision camera captures the propeller's position, further validating the TBLS signal. Movie S1 (Supporting Information) presents the ROV's visual perception under varying lighting conditions and demonstrates the TBLS's capability to detect wake with minimal reliance on vision sensors. These findings underscore the significance of integrating TBLS into ROVs to enhance wake sensing in low-visibility underwater environments.

To evaluate the reliability of the TBLS integrated into the ROV for sensing wake characteristics, experiments were conducted using an underwater propeller device, as shown in Figure 5e. The ROV remained stationary at the initial position (①) before initiating motion. At 1.4 s (T_1), the ROV commenced movement. As it reversed along the negative x-axis, it entered the wake region at 2.2 s (T_2) and exited at 4.4 s (T_3). At a distance from the wake source, the TBLS generated a voltage signal of 0.04 V with a signal period of $\Delta T_1 = 2.2$ s (light blue). The ROV continued sensing wake characteristics as it approached the underwater propeller. At 21.0 s, the ROV reversed direction and move along the positive x-axis. Since this motion opposed the previous phase, the TBLS generated waveforms with opposite trends. At 27.4 s (T_4), the ROV re-entered the wake region, and the TBLS registered a wake-induced voltage of 0.09 V. This increased voltage indicates the ROV's approach toward the wake source. The ROV exited the wake region at 28.6 s (T_5), during which the TBLS generated signals with a period of $\Delta T_2 = 1.2$ s (pink). The reduction in signal period corroborates this observation. The inset in Figure 5e

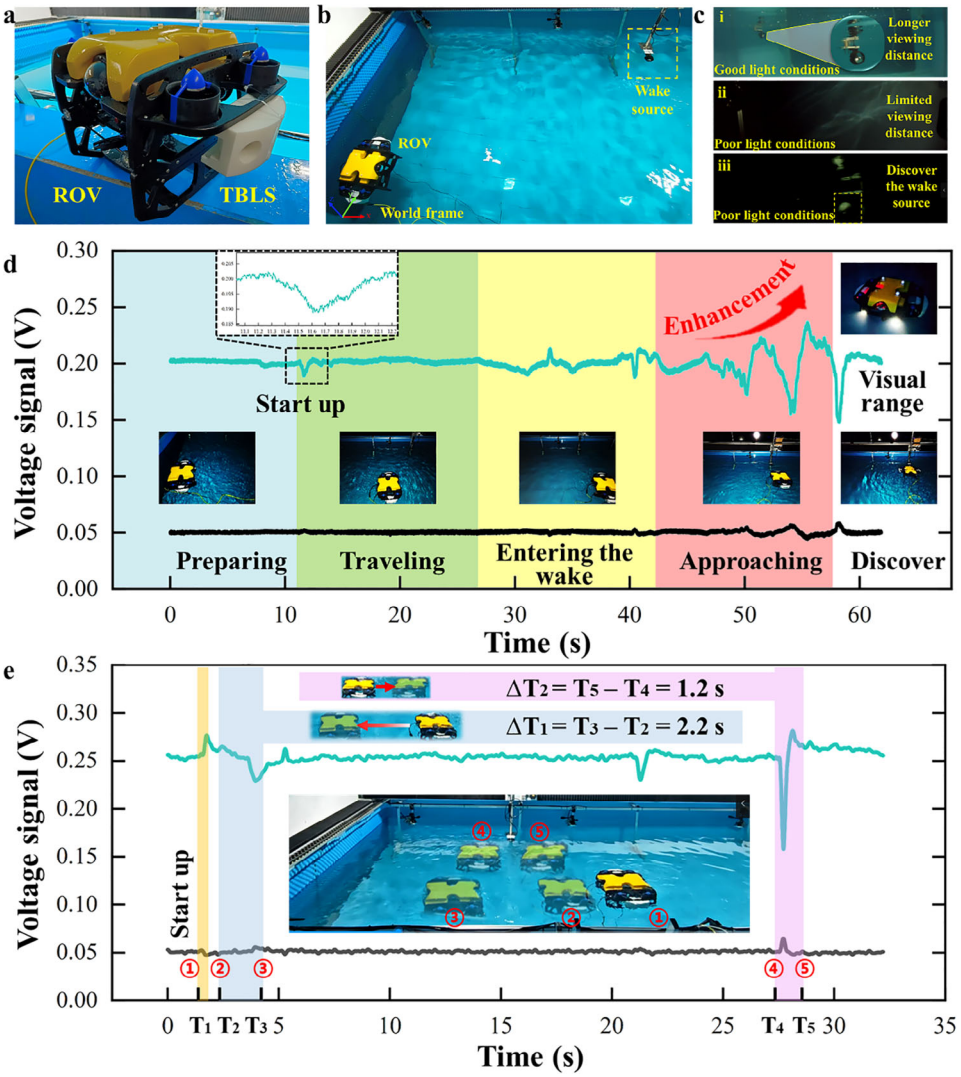

Figure 5. Demonstration of ROV with integrated TBLS in sensing flow field characteristics. a) Schematic diagram of TBLS integrated into ROV. b) Experimental scene diagram. c) Perception states of visual sensor in different underwater environments. Underwater view in i) good light conditions and ii-iii) in low light conditions. d) The whole process of sensing the wake under dark conditions and e) wake characterization.

marks the ROV trajectory positions where perceptual signals are detected, with the first phase spanning from ② to ③ and the second from ④ to ⑤. The ROV's positional data reveal that the wake generated by the propeller expands in space, forming a gradually widening "horn" shape. These results further validate the simulation findings and experimental tests presented in the previous section. Movie S2 (Supporting Information) illustrates the TBLS wake-sensing process. Additionally, the TBLS signal waveform can be used to determine the ROV's movement direction. Thus, the TBLS demonstrates strong compatibility with ROVs and effectively detects the wake characteristics of underwater propellers.

The complex underwater environment and visual blind spots inevitably impact the ability of ROVs to perceive underwater flow fields. To address this challenge, we designed a USV-ROV monitoring platform to detect underwater environmental disturbances. **Figure** 6a shows the flowchart for acquiring and transmitting disturbance information using a USV, a ROV, and a signal transmission module. Figure 6d shows a scene diagram, including the USV-ROV monitoring platform, a signal receiver and an underwater disturbance source. Figure 6f shows a close-up view of the USV-ROV monitoring platform. As shown in Figure 6g, the signal transmitters of the TBLS are mounted on the USV. Figure 6h depicts a propeller installed on an underwater telescopic rod, serving as an underwater disturbance source. Movie S3 (Supporting Information) demonstrates that when the ROV does not pass near the disturbance source, the TBLS does not generate an electrical signal. Consequently, the Arduino Nano at the transmitter fails to detect the signal, preventing the initiation of LoRa transmission. However, as the ROV continues to operate, its flank senses disturbance in the underwater flow field. Once the TBLS reaches the preset threshold voltage, the signal is transmitted, and the receiver receives an alarm message, as shown in Figure 6b. Figure 6c further indicates that when

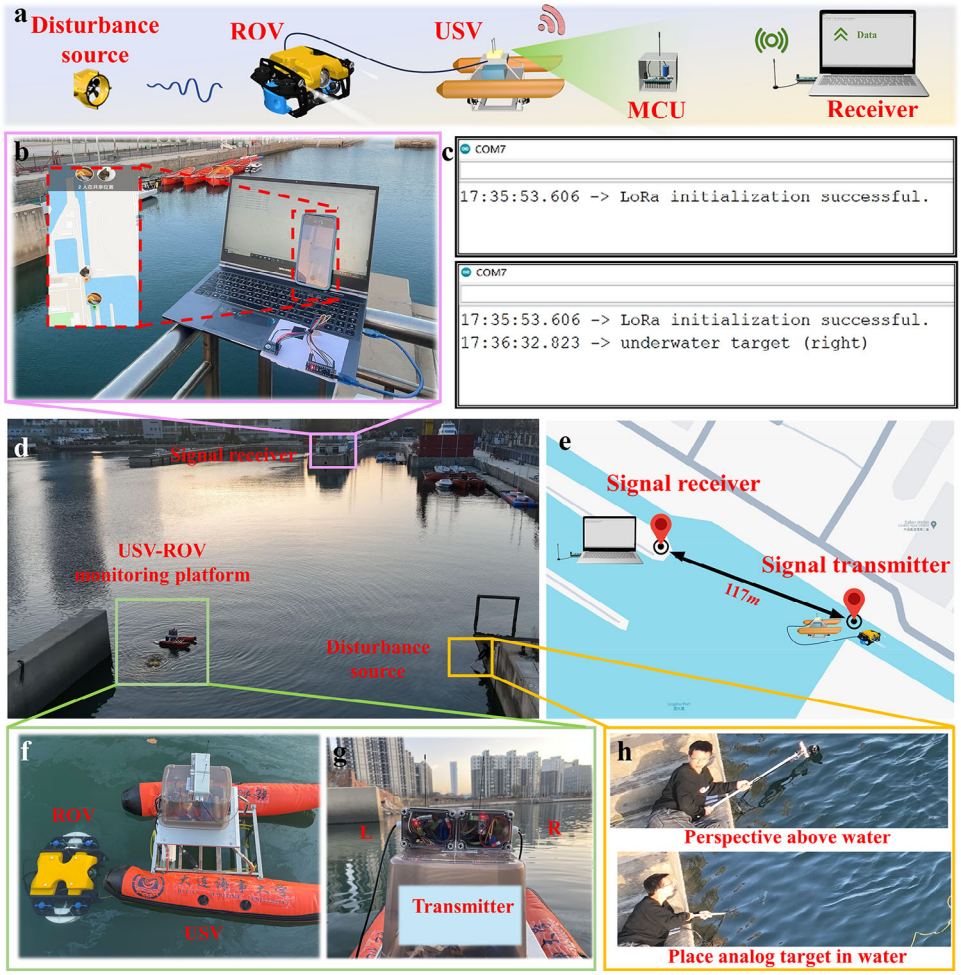

Figure 6. Application of ROV-USV monitoring platform for underwater disturbance perception. a) Flowchart of underwater information acquisition and delivery for TBLS. b) Schematic diagram of signal receiving end. c) Interface of the serial monitor on the receiving end. d) Actual Test Scene Diagram. e) Geographic location of the signal receiving and transmitting ends. f) Schematic diagram of USV and ROV. g) Signal transmitter connected to the two TBLSs carried by the ROV. h) Simulation of underwater disturbance source.

the right-side TBLS senses a disturbance, the serial display "underwater target (right)", signifying the presence an underwater disturbance source on the ROV's right side. As the ROV moves closer to the disturbance source, the receiver receives the "underwater target (right)" signal twice more, confirming the presence of the disturbance source. The inset in Figure 6b provides a zoomed-in view of the real-time location information of these two instances. As shown in Figure 6e, the measured distance between the receiving and transmitting ends is 117 meters, demonstrating the effectiveness of TBLS in enhancing ROV's underwater environment perception.

3. Conclusion

This paper presents a bionic lateral line sensor based on a triboelectric nanogenerator, designed to improve underwater vehicle's ability to recognize diverse flow fields in complex environments. The TBLS detects the spatial characteristics of propeller-generated wake fields, including horizontal distance, vertical height, incoming flow angle, and motion direction relative to the wake. The measurement error rate for the wake's characteristic thickness is only 5.7%. Additionally, the TBLS exhibits a sensitivity of 2.1 mV Pa m^{-1} in identifying oscillating flow, which is three orders of magnitude higher than previously reported values.[36] H2O AutoML is utilized to classify and identify oscillating flow signals, achieving an accuracy of 100%. Ultimately, TBLS is integrated into a ROV to enhance its ability to perceive underwater flow field disturbances in low-light conditions, compensating for the limited perception range of visual sensors. Further analysis of signal period and amplitude enhances the ROV's perception capability. Leveraging the exceptional underwater perception capabilities of TBLS, a set of wireless signal transmitters was designed for integration into the USV. An underwater flow field disturbance perception experiment was successfully conducted with the ROV in real sea conditions, where the transmitter relayed information over a distance of 117 meters after detecting underwater disturbances. This work introduces a novel underwater perception method, significantly improving the perception capabilities of underwater vehicles.

4. Experimental Section

Fabrication of the TBLS: The flexible sensing unit was a laminated structure, as shown in Figure S10 (Supporting Information). The outer layer consists of a 3 mm thick waterproof silicone casing made of Ecoflex00-10. First, 15 ml of the base material and curing agent were mixed in a container. The mixture was then placed in a vacuum pump at 0.1 MPa for degassing. Afterward, it was injected into a mold and cured in an oven at 60 °C for 5 h before being removed. Next, a rectangular CPP shielding layer, a conductive ink dielectric layer, and an FEP film polished with 10 000-grit sandpaper were sequentially arranged and embedded in the silicone layer. The interface was encapsulated with high-temperature-melted RVA resin and further sealed with a kraft paper waterproof adhesive in a two-step process. Finally, the flexible sensing unit was integrated with the bionic lateral-line canal to complete the TBLS design.

Electric Measurement and Characterization: For the wake sensing experiment of the TBLS, an underwater towing system equipped with a 750 W servo motor operating at a rotational speed of 3000 r min^{-1} was used. The system had outer dimensions of ≈6 m × 4 m and a maximum *z*-axis depth of ≈1 m. An oscillating flow experimental platform was constructed using a linear motor, as shown in Figure S11 (Supporting Information). As depicted in Figure S12 (Supporting Information), a VKINGING ELECTRONICS (SHENZHEN) Co., LTD amplifier module was used for signal conditioning. An AD7606 multichannel analog-to-digital converter was used for data acquisition. The voltage signals were evaluated by a STM32 microcontroller. As shown in Figure S13 (Supporting Information), field emission scanning electron microscopy (OLS4000) was used to characterize the surface morphology of the polished FEP.

Design of Wireless Transmitter Device: Three sets of Arduino Nano and LoRa sx1278 with a frequency band of 433 MHz were used as the transmitter and receiver for the signal transmission module. Two of these sets, powered by 18 650 batteries, were mounted on the USV as transmitters to sense underwater disturbance source on both sides of the ROV. Meanwhile, the Arduino Nano served as the signal acquisition and processing unit for the TBLS, sampling the ADC voltage value of the TBLS on the ROV via the analog pin A0. When the voltage value on a specific side exceeded the preset threshold, the corresponding alarm signal "underwater target (right/left)" was transmitted via LoRa communication to a remote receiver on shore. The Arduino Nano controlled the signal lamp alarm using digital pin D3. The receiver computer simultaneously read alarm signals from both transmitters via the Arduino IDE serial monitor through a direct data cable connection.

Supporting Information

Supporting Information is available from the Wiley Online Library or from the author.

Acknowledgements

J.L., B.L., Z.X. contributed equally to this work. This work was supported in part by the National Natural Science Foundation of China (52401399, 52371345), the Xingliao Talent Plan Young Talent Project of Liaoning Province (XLYC2203175), the Postdoctoral Fellowship Program of China Postdoctoral Science Foundation (GZC20230062), the Fundamental Research Funds for the Central Universities (No. 3132024218).

Conflict of Interest

The authors declare no conflict of interest.

Data Availability Statement

The data that support the findings of this study are available from the corresponding author upon reasonable request.

Keywords

bionic lateral-line sensor, flow recognition, triboelectric nanogenerators, underwater vehicle

Received: January 10, 2025
Revised: March 7, 2025
Published online:

[1] G. Li, X. Chen, F. Zhou, Y. Liang, Y. Xiao, X. Cao, Z. Zhang, M. Zhang, B. Wu, S. Yin, Y. Xu, H. Fan, Z. Chen, W. Song, W. Yang, B. Pan, J. Hou, W. Zou, S. He, X. Yang, G. Mao, Z. Jia, H. Zhou, T. Li, S. Qu, Z. Xu, Z. Huang, Y. Luo, T. Xie, J. Gu, et al., *Nature* **2021**, *591*, 66.
[2] J. Li, G. Zhang, C. Jiang, W. Zhang, *Ocean Eng.* **2023**, *285*, 115359.
[3] Y. C. Pan, Z. Dai, H. Ma, J. Zheng, J. Leng, C. Xie, Y. Yuan, W. Yang, Y. Yalikun, X. Song, C. B. Han, C. Shang, Y. Yang, *Nat. Commun.* **2024**, *15*, 6133.
[4] S. A. Fattah, F. Abedin, M. N. Ansary, M. A. Rokib, N. Saha, C. Shahnaz, In *2016 IEEE Region 10 Conference (TENCON)*, IEEE, Singapore **2016**, pp. 3280–3283.
[5] X. Cao, W. Liu, L. Ren, *IEEE Trans. Intell. Veh.* **2024**, 1.
[6] D. R. Yoerger, A. F. Govindarajan, J. C. Howland, J. K. Llopiz, P. H. Wiebe, M. Curran, J. Fujii, D. Gomez-Ibanez, K. Katija, B. H. Robison, B. W. Hobson, M. Risi, S. M. Rock, *Sci. Robot.* **2021**, *6*, 1901.
[7] B. Zhang, D. Ji, S. Liu, X. Zhu, W. Xu, *Ocean Eng.* **2023**, *273*, 113861.
[8] T. Wang, H.-J. Joo, S. Song, W. Hu, C. Keplinger, M. Sitti, *Sci. Adv.* **2023**, *9*, eadg0292.
[9] R. Luo, C. Li, F. Wang, *Ocean Eng.* **2024**, *303*, 117757.
[10] J. D. Tucker, M. R. Azimi-Sadjadi, *IEEE J. Oceanic Eng.* **2011**, *36*, 37.
[11] K. Iqbal, M. Odetayo, A. James, R. A. Salam, A. Z. H.j Talib, *in 2010 IEEE International Conference on Systems, Man and Cybernetics*, IEEE, Istanbul, Turkey **2010**, pp. 1703–1709.
[12] Y. Guo, H. Li, P. Zhuang, *IEEE J. Oceanic Eng.* **2020**, *45*, 862.
[13] X. Guo, Y. Li, W. Hong, Z. Yan, Z. Duan, A. Zhang, X. Zhang, C. Jin, T. Liu, X. Li, J. He, Q. Hong, Y. Xu, Y. Zhao, *ACS Sustainable Chem. Eng.* **2024**, *12*, 4835.
[14] T. Zhang, Y. Zhao, Q. Long, X. Zhu, L. He, Z. Li, X. Qian, X. He, J. Li, C. Lv, Y. Zha, Y. Chen, W. Hong, Q. Hong, X. Guo, *Chem. Eng. J.* **2024**, *497*, 154972.
[15] Y. Li, Z. Guo, X. Zhao, S. Liu, Z. Chen, W.-F. Dong, S. Wang, Y.-L. Sun, X. Wu, *Nat. Commun.* **2024**, *15*, 2906.
[16] A. G. P. Kottapalli, M. Asadnia, J. Miao, M. S. Triantafyllou, *Biomimetic Microsensors Inspired by Marine Life*, Springer International Publishing, Cham **2017**.
[17] E. Kanhere, N. Wang, A. G. P. Kottapalli, M. Asadnia, V. Subramaniam, J. Miao, M. Triantafyllou, *Bioinspir. Biomim.* **2016**, *11*, 056007.
[18] R. W. Iv, N. Neubarth, M. E. Hale, *Nat. Commun.* **2013**, *4*, 1729.
[19] X. Zheng, A. M. Kamat, A. O. Krushynska, M. Cao, A. G. P. Kottapalli, *Adv. Funct. Mater.* **2022**, *32*, 2207274.
[20] L. Guo, J. Liu, G. Wu, P. Xu, S. Wang, B. Liu, Y. Li, T. Guan, H. Wang, J. Si, T. Du, M. Xu, *Sens. Actuators, A.* **2024**, *365*, 114875.
[21] P. Xu, J. Liu, B. Liu, Y. Li, H. Jin, Z. Mu, T. Guan, G. Xie, H. Wang, M. Xu, *Nano Energy* **2024**, *129*, 110011.
[22] J. Liu, P. Xu, J. Zheng, X. Liu, X. Wang, S. Wang, T. Guan, G. Xie, M. Xu, *Nano Energy* **2022**, *101*, 107633.
[23] S. Wang, P. Xu, X. Wang, J. Zheng, X. Liu, J. Liu, T. Chen, H. Wang, G. Xie, J. Tao, M. Xu, *Nano Energy* **2022**, *97*, 107210.
[24] T. Wang, T. A. Kent, S. Bergbreiter, *arXiv:2307.04370* **2023**.
[25] Y. Zhai, X. Zheng, G. Xie, *J. Bionic. Eng.* **2021**, *18*, 264.
[26] T. Shizhe, *Microsyst. Technol.* **2014**, *20*, 2123.
[27] M. Krieg, K. Nelson, K. Mohseni, *Nat. Mach. Intell.* **2019**, *1*, 216.

[28] Q. Wang, P. Xiao, W. Zhou, Y. Liang, G. Yin, Q. Yang, S.-W. Kuo, T. Chen, *Nano-Micro Lett.* **2022**, *14*, 62.
[29] S. Shu, T. Wang, J. He, P. Chen, S. Xu, C. Li, M. Xu, W. Tang, *Device* **2023**, *1*, 100175.
[30] H. Zhang, Z. Yan, T. Zhang, J. Wang, X. Wang, Y. Chen, S. Zhu, Z. Li, Y. Chen, W. Hong, Y. Zhao, S. Chen, Q. Hong, Y. Xu, X. Guo, *ACS Sens.* **2024**, *9*, 3947.
[31] X. Guo, X. Zhu, Q. Long, X. Wu, Z. Li, J. Li, T. Zhang, X. Qian, X. Li, Y. Chen, S. Zhu, W. Hong, Q. Hong, Y. Zhao, *J. Colloid Interface Sci.* **2025**, *678*, 1061.
[32] S. He, J. Dai, D. Wan, S. Sun, X. Yang, X. Xia, Y. Zi, *Sci. Adv.* **2024**, *10*, eado6793.
[33] Z. L. Wang, *ACS Nano* **2013**, *7*, 9533.
[34] F.-R. Fan, Z.-Q. Tian, Z. L. Wang, *Nano Energy* **2012**, *1*, 328.
[35] Y. Pang, T. He, S. Liu, X. Zhu, C. Lee, *Adv. Sci.* **2024**, *11*, 2306574.
[36] J. Liu, P. Xu, B. Liu, Y. Li, T. Guan, P. Zhu, Z. Meng, S. Wang, H. Wang, M. Xu, *Small* **2023**, *20*, 2308491.
[37] P. Wu, F. Wang, S. Xu, T. Liu, Y. Qi, X. Zhao, C. Zhang, X. Mu, *Adv. Sci.* **2023**, *10*, 2301199.
[38] S. Li, D. Liu, Z. Zhao, L. Zhou, X. Yin, X. Li, Y. Gao, C. Zhang, Q. Zhang, J. Wang, Z. L. Wang, *ACS Nano* **2020**, *14*, 2475.
[39] P. Chen, J. An, R. Cheng, S. Shu, A. Berbille, T. Jiang, Z. L. Wang, *Energy Environ. Sci.* **2021**, *14*, 4523.
[40] Z. Wang, J. An, J. Nie, J. Luo, J. Shao, T. Jiang, B. Chen, W. Tang, Z. L. Wang, *Adv. Mater.* **2020**, *32*, 2001466.
[41] Y. Zou, P. Tan, B. Shi, H. Ouyang, D. Jiang, Z. Liu, H. Li, M. Yu, C. Wang, X. Qu, L. Zhao, Y. Fan, Z. L. Wang, Z. Li, *Nat. Commun.* **2019**, *10*, 2695.
[42] P. Xu, J. Zheng, J. Liu, X. Liu, X. Wang, S. Wang, T. Guan, X. Fu, M. Xu, G. Xie, Z. L. Wang, *Research* **2023**, *6*, 0062.
[43] S. Wang, P. Xu, J. Liu, H. Wang, J. Si, J. Deng, M. Xu, Z. L. Wang, *Nano Energy* **2023**, *118*, 109018.
[44] X. Zhang, M. Yu, Z. Ma, H. Ouyang, Y. Zou, S. L. Zhang, H. Niu, X. Pan, M. Xu, Z. Li, Z. L. Wang, *Adv. Funct. Mater.* **2019**, *29*, 1900327.
[45] J. An, Z. Wang, T. Jiang, P. Chen, X. Liang, J. Shao, J. Nie, M. Xu, Z. L. Wang, *Mater. Today* **2020**, *41*, 10.
[46] Y. Hou, X. Dong, D. Li, D. Shi, W. Tang, Z. L. Wang, *Adv. Funct. Mater.* **2023**, *33*, 2305719.
[47] X. Wang, Y. Shi, P. Yang, X. Tao, S. Li, R. Lei, Z. Liu, Z. L. Wang, X. Chen, *Small* **2022**, *18*, 2107232.
[48] C. Zhang, Y. Hao, J. Yang, W. Su, H. Zhang, J. Wang, Z. L. Wang, X. Li, *Adv. Energy Mater.* **2023**, *13*, 2300387.
[49] Y. Zhang, Y. Li, R. Cheng, S. Shen, J. Yi, X. Peng, C. Ning, K. Dong, Z. L. Wang, *Research* **2022**, *2022*, 9809406.
[50] P. Xu, J. Liu, X. Liu, X. Wang, J. Zheng, S. Wang, T. Chen, H. Wang, C. Wang, X. Fu, G. Xie, J. Tao, M. Xu, *npj Flex Electron* **2022**, *6*, 25.
[51] G. A. Hamill, C. Kee, *Ocean Eng.* **2016**, *124*, 104.
[52] M. Asadnia, A. G. P. Kottapalli, Z. Shen, J. Miao, M. Triantafyllou, *IEEE Sensors J.* **2013**, *13*, 3918.
[53] Y. Yang, A. Klein, H. Bleckmann, C. Liu, *Appl. Phys. Lett.* **2011**, *99*, 023701.